

Cite this: DOI: 00.0000/xxxxxxxxxx

MoS₂ bulk/monolayers van der Waals homostructures: luminescence properties and optical anisotropy

Lyubov V. Kotova,^{*a} Maxim V. Rakhlin,^a Aidar I. Galimov,^a Ilya A. Eliseyev,^a Alexey V. Platonov,^a Demid A. Kirilenko,^a Alexander V. Poshakinskiy,^a and Tatiana V. Shubina^aReceived Date
Accepted Date

DOI: 00.0000/xxxxxxxxxx

We investigated multilayer plates made by exfoliation from a high-quality MoS₂ crystal and found that they represent a van der Waals homostructure consisting of a bulk core and a few monolayers on its surface. This architecture comprising elements with different electron band structure leads to specific luminescence, when the broad emission band from the core is cut by the absorption peaks of strong exciton resonances in the monolayers. The exfoliated flakes exhibit strong optical anisotropy. We have observed a conversion of normally incident light polarization to 15 % in transmission geometry. This background effect is due to fluctuations of the *c* axis relative to the normal, whereas the pronounced resonance contribution is explained by the polarization anisotropy of excitons localized in monolayer bands.

1 Introduction

Transition metal dichalcogenides (TMDC) are among the main materials for modern physics of two-dimensional (2D) semiconductors since 2005, when it was demonstrated that stable free-standing atomic crystals can be obtained by micromechanical cleavage (exfoliation)¹. Among the TMDC family, the molybdenum disulfide (MoS₂) occupies a special place as one of the most studied layered compound which in addition is stable under ambient conditions and can be easily synthesized. The 2D MoS₂ was investigated for various applications in nanophotonics owing its unique features such as the extremely high exciton binding energy of hundreds of meV and the radiation time of a few picoseconds^{2,3}. Moreover, van der Waals (vdW) heterostructures⁴ containing MoS₂ monolayers were successfully created⁵⁻⁷. These provide an ideal platform for both fundamental research and new device invention.

Theoretically, it has been predicted that the band gap of bulk MoS₂ is indirect being in the near infrared range (~1.3 eV)⁸, whereas the band gap of a 2D monolayer is direct (~1.8 eV) and occurs at the high-symmetry point K^{9,10} of the Brillouin zone. It is important to emphasize that the absorption spectra measured in multilayer MoS₂ plates have two strong resonances in the 1.8-2.1 eV range, associated with A and B direct excitons^{11,12}. As expected, no features were observed near the indirect band gap. However, an unexpected fact is the lack of data on near-band-edge emission in the bulk MoS₂ crystals that might be near 1.3

eV. Only weak PL lines attributed to intercalated halogen atoms and deep donor centers were previously observed between 0.8 and 1.2 eV¹³. The development of the micro-photoluminescence (micro-PL) spectroscopy, which provides a much higher excitation power, made it possible to obtain experimental confirmation of the transformation of the band structure in the monolayer limit. It showed that a monolayer does exhibit one emission band near 1.9 eV, while stacks of few monolayers (up to 6) demonstrated both direct and indirect PL bands at 1.9 eV and 1.3 eV of much lower intensity^{14,15}. It was suggested that the presence of the disorder in the investigated natural crystals provides the broadening of PL spectra^{16,17}. Mechanical stress can also lead to polarization splitting of the exciton peaks¹⁸. Our recent micro-PL studies showed that such two PL bands exist in nanostructures consisting of several tens of monolayers; however, indirect radiation is completely extinguished at low temperatures¹⁹. This phenomenon, which requires further study, is probably associated with the temperature balance between fast direct and slow indirect exciton transitions, as well as with the possible contribution of dark exciton states²⁰. One can assume that modern spectroscopy can shed light on the optical properties of bulk structures with hundreds or thousands of monolayers, which are the parent materials for 2D nanostructures.

The widely used exfoliation method inevitably means stressing and bending of a plate that weaken the bonds between the layers, especially between those which are superficial in relation to the rest of the bulk core. A change in the dielectric environment and in the magnitude of the van der Waals gap can lead to the transformation of the local band structure of the superficial monolayers²¹. Besides, the enhanced strain and bending during

^a Ioffe Institute, St. Petersburg, 194021, Russia. E-mail: kotova@mail.ioffe.ru

† Electronic Supplementary Information (ESI) available: [details of any supplementary information available should be included here]. See DOI: 00.0000/00000000.

the mechanical cleavage can cause the formation of oriented extended defects such as ripplocations and hyperdislocations^{22,23}. They separate the layers into domains that is the basic reason of the extremely small size of monolayers fabricated by the exfoliation method (tens of microns only).

In this work, we have studied samples of micrometer thickness prepared by exfoliation. Measured luminescence spectra with sharp dips at the energies of A and B exciton resonances, as well as in-plane optical anisotropy in transmission, show that we are dealing with a new object *van der Waals homostructures*, consisting of a bulk core and monolayers on its surface. The appearance of homostructures of one material MoS₂ is possible due to the sharp difference between the band structures of the monolayer and the bulk material. The study of the optical properties of such homostructures opens up the possibility of obtaining data on the main characteristics of both a bulk material and a 2D monolayer located on a related semiconductor matrix.

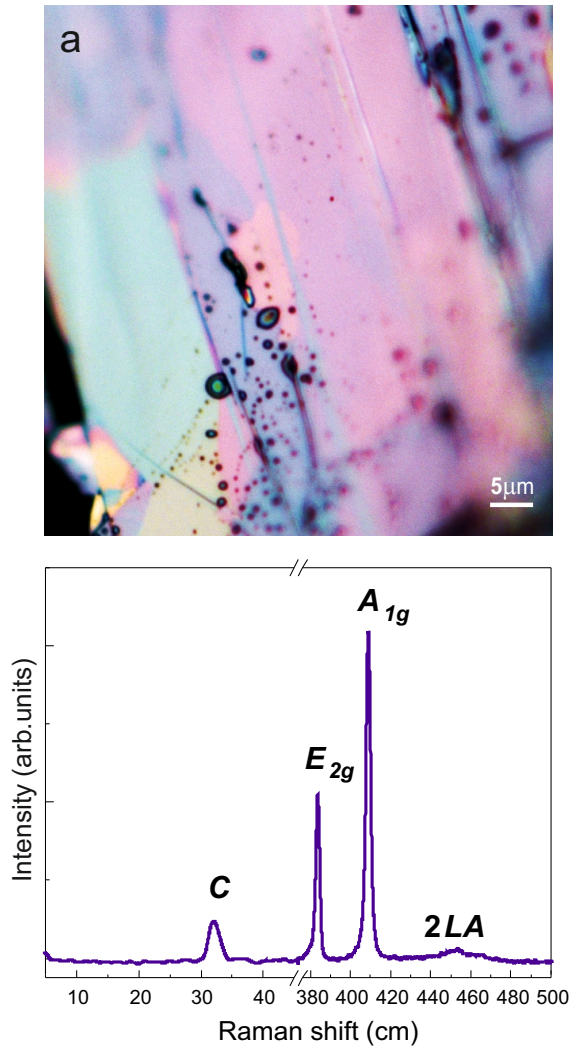


Fig. 1 a) Optical microscope image of a sample exfoliated from the bulk MoS₂ crystal using adhesive-tape method (the bubbles are likely traces of the adhesive tape). b) A Raman spectrum measured at 300 K, which is typical for the entire surface of the sample.

2 Experimental

2.1 Samples

The vdW structures under study were fabricated from a commercially available high-quality MoS₂ bulk crystal (HQ-graphene production). For sample preparation, both mechanical microcleavage and a so-called Scotch-tape method²⁴ were used. An optical microscope image of one of such flakes fabricated using adhesive tape technology is presented in Fig. 1 a. The sample surface consists of domains separated by boundaries. The thickness of the samples prepared for optical studies was determined by the interference in the transmission spectrum and equals 1 μm. Structural quality of the samples is typical for high-quality MoS₂, as confirmed by micro-Raman studies, namely: by the observed Raman peak positions and their narrow width (see Fig. 1 b). The Raman signal is identical for all detection areas. Regardless of the signal registration area, the obtained Raman spectra did not display any differences between each other. All features visible in the spectrum (Fig. 1 b), such as the C (31 cm⁻¹), E_{2g} (383 cm⁻¹) and A_{1g} (409 cm⁻¹) lines are characteristic of high-quality MoS₂^{25–27}. Frequency difference between the A_{1g} and E_{2g} Raman lines (26 cm⁻¹) corresponds to the values reported for bulk MoS₂²⁸. Presence of an interlayer C mode with a frequency of 31 cm⁻¹ together with the absence of layer-breathing modes in the 5 – 30 cm⁻¹ allows us to characterize the material as a bulk MoS₂ crystal²⁹.

To determine how the delamination process affects the crystal structure, we conducted transmission electron microscopy (TEM) studies using a Jeol JEM-2100F microscope. We will further focus on specimens produced from the bulk MoS₂ crystal by mechanical cleavage, that is a cleaner method than the adhesive tape exfoliation³⁰.

The results of the TEM studies of samples fabricated from a bulk MoS₂ crystal by mechanical cleavage are presented in Fig. 2. The image of a material fragment obtained by cleavage along the (0001) plane is given in Fig. 2 a. A cross-section TEM specimen was made from an adjacent MoS₂ fragment. The high resolution image in Fig. 2 b exhibits many extended defects. Some of them are the stacking faults and others look as seeds of ripplocations, whose chain is marked by magenta arrows. The ripplocations – internal ripples – can appear during cleaving due to the ease of bending of atomic layers and weak van der Waals bonds between them²². In layered crystals, they tend to group together³¹, promoting the formation of penetrating hyperdislocations²³. When the strain of cleaving is high, the continuous layers can be separated into domains by such extended defects.

Investigation of the fragments cleaved along the (0001) plane suggests that there is an up to 10° misorientation of various regions in the sample. This misorientation leads to the multiplication of the diffraction spots in Fig. 2 c. This feature is absent in the diffractogram of an intact flake synthesized by the chemical transport reaction method, as described in¹⁹. Diffraction patterns of the cross-sectional specimen Fig. 2 e,f obtained at different orientations correspond to the lateral (in-plane) displacement of the atomic layers. Moreover, the elongation of the diffraction spots in given patterns increases proportionally to the diffraction index. This indicates the presence of regions with markedly differ-

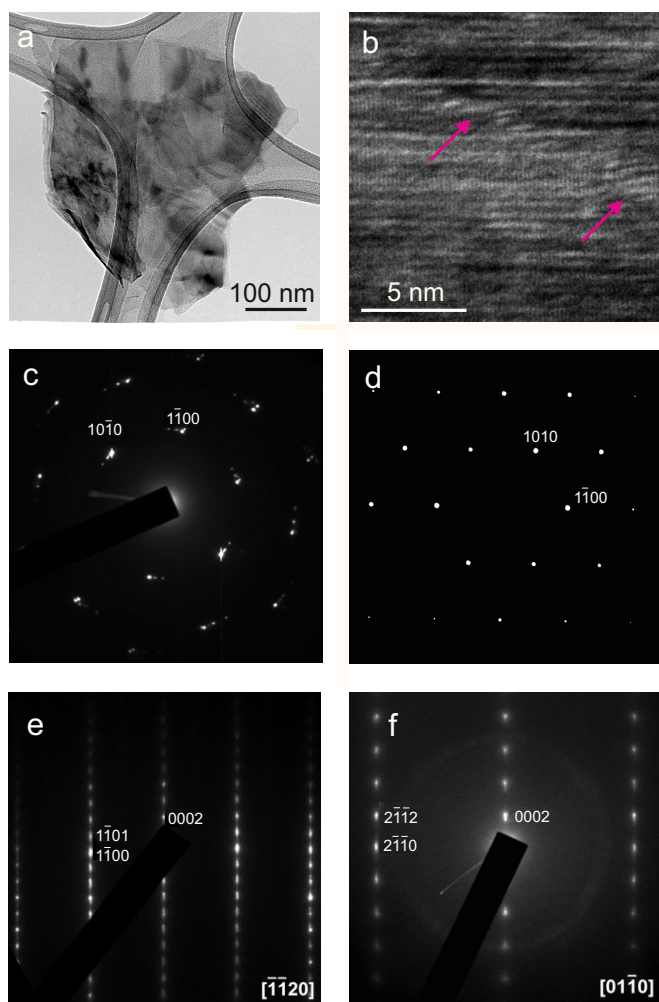


Fig. 2 a) TEM image of a flake cleaved along the (0001) plane. It lies on a carbon lacey film. b) Cross-sectional image of a multilayer specimen cut from the same bulk crystal across the layers. The arising chain of ripples is marked with magenta arrows. c), d) Diffraction patterns of (c) the mechanically cleaved flake, and (d) an uncleaved thin flake synthesized by the chemical transport reaction method. (e), (f) Electron diffraction pattern of a cleaved specimen, the same as in (b), obtained in cross-sectional geometry at various orientations indicated in the graphs.

ent interlayer spacing, at least 10% larger than the characteristic value of molybdenum disulfide. The presence of filaments near the spots of type $2\bar{1}\bar{1}0$ cannot be explained only by a change in the spacing. This assumes the contribution of the lateral displacement of the atomic layers by vectors incommensurate with the lattice period as well.

In general, the TEM results show that sample preparation provides suitable conditions not only for the formation of defects, but also for the separation of atomic layers. This trend should be more pronounced for superficial monolayers. As a result, the cleaved flakes can be viewed as homostructures consisting of a bulk MoS₂ core and monolayers/bilayers at its surface, or somewhere within the volume, that cannot be excluded. A similar architecture can be implemented in flakes exfoliated using the adhesive tape technology. To find additional facts confirming such architecture, we performed optical studies as described below.

2.2 Optical methods

Micro-photoluminescence (μ -PL) setup was used to investigate the luminescence properties of MoS₂ samples. They were mounted in a He-flow cryostat ST-500-Attocube with a XYZ piezo-driver inside, which allowed us to optimize and precisely maintain the positioning of a chosen place on the sample with respect to a laser spot. Non-resonant optical excitation of a cw Nd:YAG laser (532 nm) was used for the μ -PL measurements. Another micro-spectroscopy setup, comprising a Horiba Jobin-Yvon T64000 spectrometer with a confocal microscope and a CCD detector, was used for micro-Raman (μ R) and PL measurements at both room and liquid nitrogen temperatures. Raman spectra have been measured to characterize the quality of the samples under study. In addition, the Raman lines were recorded simultaneously while scanning the PL bands. The PL spectra were normalized to the intensity of the Raman line to exclude random variations. Spatial resolution of these measurements corresponds to an area of $\sim 1 \mu\text{m}$ in diameter.

For measurements of light transmission, a halogen lamp was used as a light source. A parallel beam of light was formed using lenses and slits. The spectra were registered with a 0.5 m monochromator and a CCD camera. All transmission measurements were performed at room temperature. The incident light was linearly polarized. Control under transmitted light polarization was achieved by means of half- and quarter-wave plates and a Glan-Taylor prism installed in the detection channel. Different polarization configurations were used. The accuracy of measuring the degree of polarization was estimated as 0.1 %. The sample holder allowed us to rotate the sample around the normal axis for obtaining the dependencies of the transmitted light polarization in a full 360° angle range.

To visualize the morphology of the samples under study, we used the optical microscope with the possibility of measuring in different polarizations. Other details of the optical techniques are given in Supplementary Materials.

3 Results and discussions

3.1 Micro-photoluminescence

The photoluminescence of MoS₂, whose thickness varies from monolayer to bulk, has been already well studied^{2,14,32–36}. Here we demonstrate that the photoluminescence of the MoS₂ vdW homostructure is very distinctive. Micro-photoluminescence spectra obtained from different points on the surface are shown in Fig. 3 a-f. The spectra are of three distinct types. Figures 3 a,b correspond to the case when the signal is collected from bulk MoS₂ core of the sample. The broad peak in the luminescence is explained by the near-band-edge transitions with some contribution of excitonic emission. On the contrary, the signal collected from the areas shown in Fig. 3 c,e features two narrow dips atop of the broad peak corresponding to bulk luminescence. In this flat area, the bulk core of the homostructure can be covered by atomically-thin MoS₂ flakes. The dips are explained by the light absorption at frequencies close to exciton resonances in these flakes, namely, A exciton at 1.94 eV and B exciton at 2.15 eV (at T=10 K). We assume that the areas described in Fig. 3 c,d

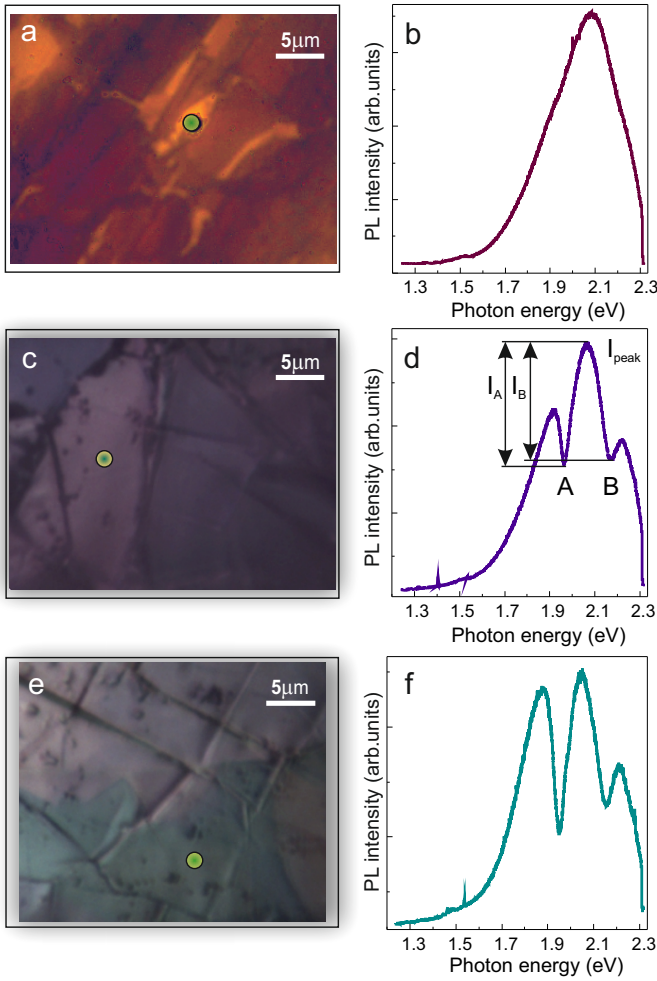


Fig. 3 a,c,e) MoS₂ flake's surface image show the area where μ -PL was excited. b,d,f) μ -PL intensity spectra. A and B excitons' positions and intensities are indicated on the plot.

and Fig. 3 e,f differ in the number of layers covering the bulk core, which leads to different amplitudes of the dips. The exciton absorption for a monolayer can be estimated as $A_1 = 2\Gamma_0/\Gamma_x$, where Γ_0 is the radiative exciton decay and Γ_x is the non-radiative broadening of exciton resonance, and $\Gamma_0 \ll \Gamma_x$ is assumed. For A exciton, using $\Gamma_0 = 1.4 \text{ meV}$ ³⁷ and $\Gamma = 30 \text{ meV}$, as extracted from the HWHM of the exciton dip (see Supplement Figure S5), we estimate that $N \sim 5$ monolayers are required to achieve the PL attenuation $(1 - A_1)^N \approx 0.6$ observed at exciton resonance. Since the surface layers make up the smaller portion of the vdW homostructure, which can be additionally being depleted in carriers, peaks corresponding to luminescence from the excitons in flakes are masked by the much stronger bulk luminescence.

In addition to the direct exciton features, the signal collected from some areas features also a peak at the indirect exciton frequency $\sim 1.3 \text{ eV}$, see Supplementary Figure S3 a,b. The dominance of the direct-gap and transitions in the spectra of multilayer structures at low temperature was previously observed in Ref.¹⁹ and explained by the fast radiative recombination of the direct excitons as compared to slow energy relaxation and phonon-

assisted recombination of indirect excitons²⁰. In addition, at a few points purely excitonic radiation dominates, as shown in the Supplementary Figure S3 c,d.

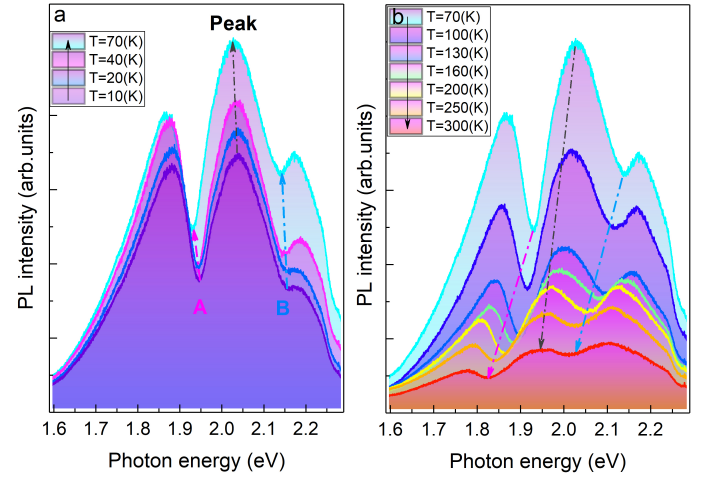


Fig. 4 a,b) μ -PL intensities at different temperature. A and B excitons positions are indicated on the plot.

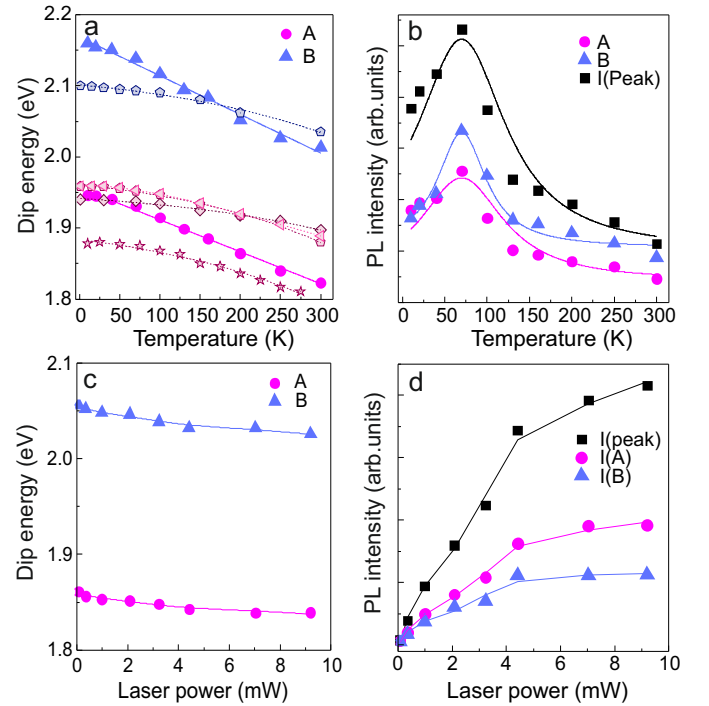


Fig. 5 a,c) Dependence of the position of A and B excitons on temperature and laser pump power. The unpainted characters represent the literature data on excitons in monolayers (triangle³⁸, rhombus³⁹, pentagon⁴⁰, hexagon⁴¹), asterisks represent the PL peak energy in the synthesized uncleaved thin flake. b,d) The μ -PL intensities dependencies on the temperature and laser pump power. Laser pump power dependency was obtained at room temperature.

We also measured the evolution of the μ -PL spectra with temperature, Fig. 4 a,b and pump power, Supplementary Figure S6. Figure 5 a-d shows dependence of the positions and intensities

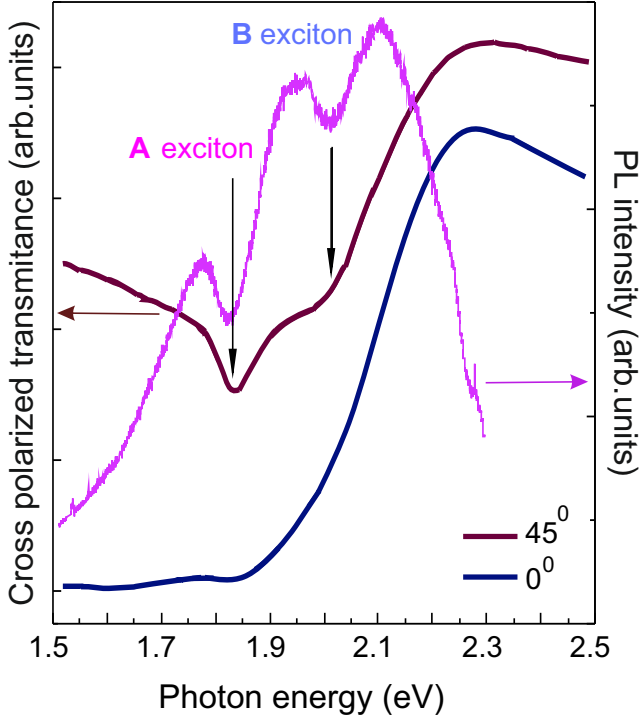


Fig. 6 The transmission spectra of the MoS₂ van der Waals homostructure in cross polarization for two angles of sample rotation measured at room temperature, shifted for clarity and shown together with a PL spectrum.

of the broad peak (bulk luminescence) and two dips (exciton absorption). The positions of the dips decrease with temperature, see Fig. 5 a, that generally agrees with the variation of the band gap. Energetically decreasing dependencies were observed in multiple previous optical absorption and PL studies, see unprinted characters in Fig. 5 a and the Supplementary Tables I and II. However, the dependencies do not match in the slope with ours, since the vdW homostructure is different from both synthesized flake, that is, the bulk material, and a stack of monolayers on different dielectric substrates. Note that the broad peak position can be determined with limited accuracy due to its complex nonsymmetric shape additionally modified by the exciton dips. The intensities of the peak and the dips increase at small temperatures, then reach maximum at around 70K and decrease at higher temperatures, see Fig. 5 b. Such behavior could indicate that the transition with lowest energy is dark in the bulk MoS₂ as was assumed in Refs.^{19,42}. In this case, the bright optical transition with higher energy starts emitting only with an increase of the temperature. The release of carrier trapped by defects could also contribute to the increase of PL at low temperatures. With an increase of the laser power the positions of the dips remain almost constant, see Fig. 5 c. A very small decrease occurs probably due to the heating by a laser beam. As a result, the intensities of the peak and the dips grow linearly and then saturate, see Fig. 5 d.

3.2 Polarization anisotropy

To quantify the optical anisotropy, we have studied how the polarization of the normally incident light changes when it is transmitted through the vdW homostructure at room temperature. As the polarization of the linearly polarized incident light was rotated with respect to the sample, the following components of the transmitted spectrum were measured: polarized along (I_{\parallel}) and perpendicular (I_{\perp}) to the incident light polarization, polarized along the axes rotated by 45° with respect to the incident light polarization ($I_{1,2}$), and polarized circularly ($I_{\sigma_{\pm}}$). From that, the full set of the Stokes parameters can be calculated according to

$$P_{\text{circ}} = \frac{I_{\sigma_+} - I_{\sigma_-}}{I_{\sigma_+} + I_{\sigma_-}}, \quad \tilde{P}_{\text{lin}} = \frac{\tilde{I}_1 - \tilde{I}_2}{\tilde{I}_1 + \tilde{I}_2}, \quad P_{\text{lin}} = \frac{I_{\perp} - I_{\parallel}}{I_{\perp} + I_{\parallel}}. \quad (1)$$

Similar approach has been used recently to study the optical activity of QWs^{43,44}.

The spectra of the transmitted light component cross polarized to the incident light I_{\perp} are shown in Fig. 6 for two orientations of incident light polarization which correspond to minimal (blue curve) and maximal (red curve) signals. The strong dependence of I_{\perp} on the incident light polarization orientation is present in a wide spectral range and indicates the in-plane optical anisotropy of the structure, i.e., the difference of the dielectric permittivities for the two in-plane directions. Such optical anisotropy can arise due to in-plane stress or shear deformation of the bulk core. Here, it is most likely caused by the anisotropic fluctuations of the flakes' c -axes directions, revealed in testing X-ray measurements (the studied sample is too small to register XRD scans). The transmitted light linear polarization degree in the axes rotated by $\pm 45^\circ$, \tilde{P}_{lin} , is found to be very small (less than 2%, see Supplementary Figure S8), which indicates that linear dichroism does not exist in the structure, i.e, the imaginary part of dielectric permittivity is isotropic in the plane of the structure.

On top of the smooth background, the cross-polarized transmittance spectra (Fig. 6) feature peculiarities at the frequencies of A and B excitons. Their positions agree with the previous investigations of MoS₂ thin crystals^{11,45-47}. To further investigate the optical properties associated with the exciton transitions in the vdW homostructure, we have measured the transmitted light circular polarization degree P_{circ} in the corresponding frequency range, see Fig. 7. Similarly to cross-polarized transmittance, the spectrum of the circular polarization degree, Fig. 7a, consists of a smooth background with two exciton peaks on top of it. Dependence of the background value and of the exciton peak amplitudes on the sample rotation angle α is shown in Figs. 7 b,c. The measured data are well described by the sine function

$$P_{\text{circ}}(\alpha) = \frac{\omega d}{2c} \text{Re}(\Delta n) \sin 2(\alpha - \alpha_0), \quad (2)$$

where d is the sample thickness, Δn is the difference between the refractive indices of the two in-plane optical axes, α_0 is the direction of one optical axis, and the direction of the other is $\alpha_0 + 90^\circ$. When the incident light is polarized along one of the optical axes, P_{circ} vanishes, while for directions rotated by $\pm 45^\circ$ with respect to them P_{circ} is maximal. The absolute value of the

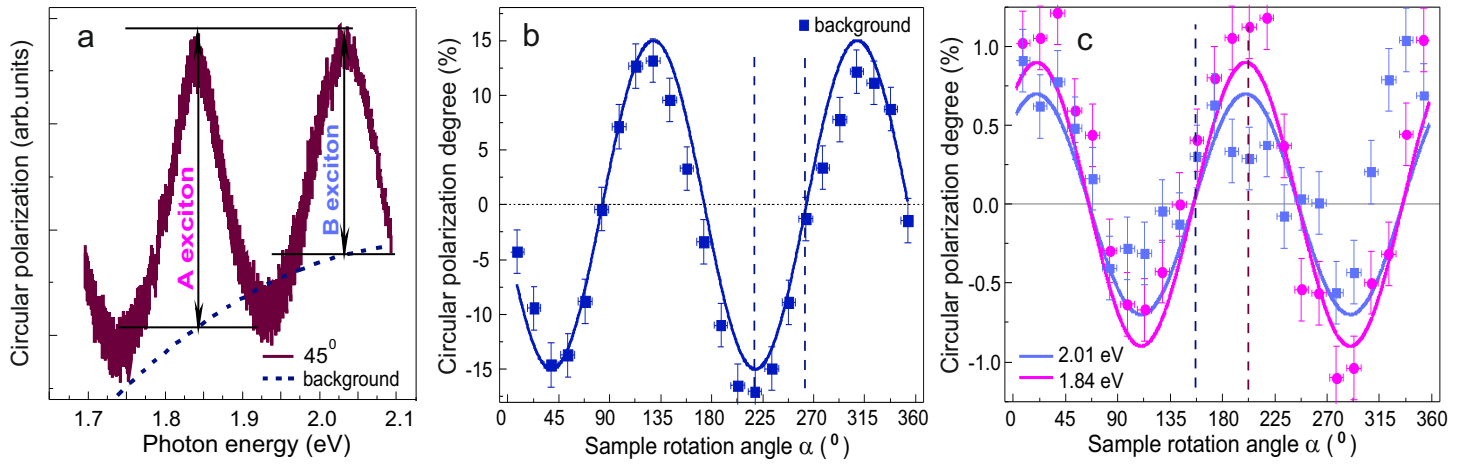


Fig. 7 a) The spectra of the transmitted light circular polarization degree for the MoS₂ vdW homostructure measured at orientation corresponding to the the maximal signal. The background signal and the amplitudes of the peaks related to A and B excitons are indicated. b) Sample orientation dependence of the P_{circ} for background signal valid in a wide spectral range. c) Sample orientation dependencies of A and B exciton peaks' amplitudes. All curves are obtained at room temperature.

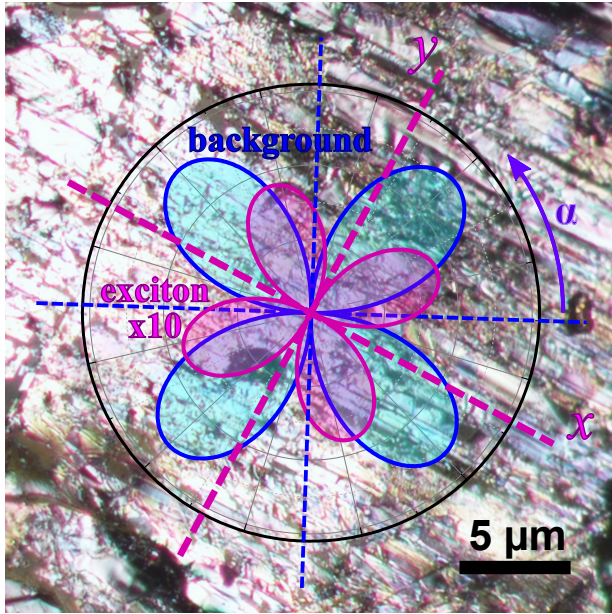


Fig. 8 MoS₂ flake's surface image with bright-field microscopy obtained by Nikon industrial microscope ECLIPSE LV150. Over it there are two polarization dependencies of transmission light through the sample. Navy blue feature corresponds to the anisotropy of bulk multilayer flake. Magenta curve corresponds to the anisotropy in the vicinity of the exciton resonance (the signal value is multiplied by 10 to facilitate comparison of directions).

circular polarization degree allows us to quantify the strength of the in-plane optical anisotropy. The background contribution is determined by the the bulk of the structure, so we use $d = 1 \mu\text{m}$ and obtain $\Delta n^{(bg)} = 1.2 \cdot 10^{-2}$. The excitonic contribution is determined only by the surface layer of the width d_x and is an order of magnitude weaker. The fit gives $\Delta n^{(x,A)} d_x = 9 \cdot 10^{-4} \mu\text{m}$ and $\Delta n^{(x,B)} d_x = 7 \cdot 10^{-4} \mu\text{m}$ for A and B excitons respectively. Using $d_x \sim 10 \text{ nm}$, we estimate $\Delta n^{(x)} \sim 0.1$.

Interestingly, the optical axis direction α_0 extracted from the

angular dependence of the exciton peak amplitude and that of the background are different, cf. the phases of the cosine in Figs. 7 b,c. As discussed in Sec. 3.1, the excitonic features are determined by the flakes on the surface of the homostructure. Therefore, we conclude that the optical axes of the surface are different from those of the bulk by $\alpha_0^{(x)} - \alpha_0^{(bg)} = 27^\circ$. To prove that, we take the picture of the surface using bright-field microscope, see Fig. 8. The image reveals that linear structural defects aligned in a certain direction are present on the surface⁴⁸. The presence of such defects is probably associated with the production of the sample using the adhesive tape method. We superpose the angular dependencies of the background and exciton contributions to the surface image, see the navy blue and magenta curves which are drawn after the corresponding curves in Figs. 7 b,c. The orientation of the exciton contribution turns out to be consistent with the direction of the structural defects: the conversion to the circular polarization vanishes when the incident light is polarized along or perpendicular to the linear defects, see the optical axes indicated by the dashed magenta lines, and reaches maximum when the incident light polarization is rotated by $\pm 45^\circ$ with respect to them.

The orientation of the linear defects, which are the fractures on the surface, most probably coincides with one of the the zigzag directions $\langle 1\bar{1}00 \rangle$, since cutting material along this direction requires breaking the smallest number of chemical bounds. Then, the axes of the background optical anisotropy, which are rotated with respect to those of the exciton contribution by the angle very close to 30° (the deviation by a few degrees is probably due to the depolarization effect that alters the background signal as it passes through the linear defects on the surface⁴⁹), are close to the crystallographic directions $\langle 11\bar{2}0 \rangle$ and $\langle 1\bar{1}00 \rangle$. The presence of distortions along such directions was revealed in the diffraction patterns of Fig. 2c-f.

3.3 The origin of the optical anisotropy

Finally, we discuss the microscopic mechanisms for the observed optical anisotropy. The background contribution can be explained by the dispersion of the c -axis direction in the bulk of the structure. Due to the birefringence of the bulk MoS₂, a tilt of the c -axis in a certain direction from the structure normal to a small angle θ , leads to in-plane optical anisotropy

$$\Delta n^{(\text{bg})} = \frac{\sqrt{\varepsilon_{\perp}}}{2} \left(1 - \frac{\varepsilon_{\perp}}{\varepsilon_{\parallel}} \right) \theta^2, \quad (3)$$

where $\varepsilon_{\parallel, \perp}$ are the dielectric constants of the bulk MoS₂ along and perpendicular to the c -axis. Using $\varepsilon_{\parallel} = 6.5$, $\varepsilon_{\perp} = 15.5$ ^{11,50} we estimate the mean square angle of c -axis tilt required to obtain the observed value of $\Delta n^{(\text{bg})}$ as $\sqrt{\langle \theta^2 \rangle} \sim 2.5^\circ$.

To explain the exciton contribution to optical anisotropy, we suppose that the excitons in the flakes on the structure surface get localized on linear defects, being able to move freely along them while confined in the perpendicular direction. The lateral confinement wave vector $K \sim \pi/l$, where $l \lesssim 1 \mu\text{m}$ is the width of the linear defect, is comparable to the light wave vector. As a result, a significant longitudinal-transverse splitting between the frequencies of excitons polarized along and perpendicular to the linear defects arises^{51,52}. The splitting value for the excitons inside the light cone depends strongly on the dielectric environment and is limited by the exciton radiative decay rate,⁵³ $\Delta\omega_x \lesssim \Gamma_0$. Due to this splitting, the refractive index acquires an in-plane anisotropy

$$\Delta n^{(x)} = -\frac{\sqrt{\varepsilon_{\perp}} \omega_{\text{LT}} \Delta\omega_x}{2(\omega - \omega_x + i\Gamma_x)^2}, \quad (4)$$

where Γ_x is the exciton width and ω_{LT} is the exciton-induced longitudinal-transverse splitting in the surface layer of the homostructure covered by MoS₂ flakes. The latter can be calculated as $\omega_{\text{LT}} = 2c\Gamma_0/(\omega a)$,⁵⁴ where Γ_0 is the radiative decay rate of a single flake and a is the distance between the flakes. Using $\Gamma_x = 50 \text{meV}$, as determined from the spectrum in Fig. 7(a) and the surface layer thickness $d_x \sim 5a$, we estimate that to obtain $\Delta n^{(x)} d_x \sim 10^{-3} \mu\text{m}$ observed in the experiment, the exciton energy splitting should be $\Delta\omega_x \sim 0.8 \text{meV}$, which is safely below the theoretical upper limit for the in-plane longitudinal-transverse splitting $\sim \Gamma_0 = 1.4 \text{meV}$.

Depolarization of the electric field inside the linear defects could result in a difference of the exciton oscillator strength along and perpendicular to the defects and result in refractive index anisotropy of the form $\Delta n^{(x)} = \sqrt{\varepsilon_{\perp}} \Delta\omega_{\text{LT}}/(\omega - \omega_x + i\Gamma_x)$. However, the corresponding contribution to circular polarization degree, determined by $\text{Re} \Delta n^{(x)}$, would have a form of the Lorentz function derivative, vanishing at exciton resonance frequency, in contradiction to a peak at exciton frequency observed in experiment.

4 Conclusion

To conclude, the van der Waals homostructure consisting of a bulk core and several flakes of monolayer thickness on its surface was fabricated and investigated. This architecture, consisting of elements with different structures of electronic bands, leads

to specific luminescence spectrum: the broad emission band of the bulk core is cut off by the absorption peaks of strong exciton resonances in monolayers. We have studied the optical transmission of MoS₂ vdW structures and revealed their polarization anisotropy leading to polarization conversion. The effect consists of two contributions: (i) background anisotropy due to linear birefringence of the bulk crystal and the fluctuations of the c -axis direction and (ii) longitudinal-transverse splitting of the exciton energies due to their localization by the structural defects on the sample surface. The bulk contribution leads up to 15% linear-to-circular polarization conversion per micron of sample thickness. The exciton contribution is one order of magnitude smaller and its angular dependence is consistent with the direction of linear structural defects on the sample surface.

Conflicts of interest

There are no conflicts to declare.

Acknowledgements

This work is supported by the Russian Science Foundation (project No. 19-12-00273). We thank M. Remškar for supplying the synthesized MoS₂ flakes and M. A. Yagovkina for testing X-ray measurements. The sample characterizations by TEM and polarization microscopy were done at the Joint Research Center “Material science and characterization in advanced technology” (Ioffe Institute, St.-Petersburg, Russia).

Notes and references

- 1 K. Novoselov, D. Jiang, F. Schedin, T. Booth, V. Khotkevich, S. Morozov and A. Geim, *Proc. Natl. Acad. Sci. U.S.A.*, 2005, **102**, 10451.
- 2 G. Wang, A. Chernikov, M. Glazov, T. Heinz, X. Marie, T. Amand and B. Urbaszek, *Rev. Mod. Phys.*, 2018, **90**, 021001.
- 3 M. Durnev and M. Glazov, *UFN*, 2018, **188**, 913.
- 4 A. Geim and I. Grigorieva, *Nature*, 2013, **499**, 419–425.
- 5 Y. Gong, J. Lin, XingliWang, G. Shi, S. Lei, Z. Lin, X. Zou, G. Ye, R. Vajtai, B. I. Yakobson, H. Terrones, M. Terrones, B. K. Tay, J. Lou, S. T. Pantelides, Z. Liu, W. Zhou and P. M. Ajayan, *Nature Materials*, 2014, **13**, 1135.
- 6 W. Yang, H. Kawai, M. Bosman, B. Tang, J. Chai, W. L. Tay, J. Yang, H. L. Seng, H. Zhu, H. Gong, H. Liu, K. E. J. Goh, S. Wang and D. Chi, *Nanoscale*, 2018, **10**, 22927–22936.
- 7 *Two Dimensional Transition Metal Dichalcogenides*, ed. N. S. Arul and V. D. Nithya, Springer, Singapore, 1st edn, 2019.
- 8 L. F. Mattheiss, *Phys. Rev. Lett.*, 1973, **30**, 784.
- 9 T. Li and G. Galli, *J. Phys. Chem. C*, 2007, **111**, 16192–16196.
- 10 S. Lebegue and O. Eriksson, *Phys. Rev. B*, 2009, **79**, 115409.
- 11 B. Evans and P. Young, *Proc. R. Soc. Lond. A*, 1965, **284**, 402–422.
- 12 R. A. Nevill and B. L. Evanst, *phys. stat. sol. (b)*, 1976, **78**, 597.
- 13 L. Kulyuk, L. Charron and E. Fortin, *Phys. Rev. B*, 2003, **68**, 075314.

- 14 K. F. Mak, C. Lee, J. Hone, J. Shan and T. F. Heinz, *Phys. Rev. Lett.*, 2010, **105**, 136805.
- 15 A. Splendiani, L. Sun, Y. Zhang, T. Li, J. Kim, C.-Y. Chim, G. Galli and F. Wang, *Nano Lett.*, 2010, **10**, 1271–1275.
- 16 K. Gołasa, M. Grzeszczyk, K. Korona, R. Božek, J. Binder, J. Szczytko, A. Wyszomolek and A. Babiński, *Acta Physica Polonica A*, 2013, **124**, 849–851.
- 17 R. Dhall, M. R. Neupane, D. Wickramaratne, M. Mecklenburg, Z. Li, C. Moore, R. K. Lake and S. Cronin, *Adv. Mater.*, 2015, **27**, 1573–1578.
- 18 A. Mitioglu, J. Buhot, M. V. Ballottin, S. Anghel, K. Sushkevich, L. Kulyuk and P. C. M. Christianen, *Phys. Rev. B*, 2018, **98**, 235429.
- 19 T. Shubina, M. Remskar, V. Davydov, K. Belyaev, A. Toropov and B. Gil, *Ann. Phys. (Berlin)*, 2019, **531**, 1800415.
- 20 O. O. Smirnova, I. A. Eliseyev, A. V. Rodina and T. V. Shubina, *Journal of Physics: Conference Series*, 2020, **1482**, 012038.
- 21 H. Peelaers and C. V. de Walle, *Phys Rev B*, 2012, **86**, 241401.
- 22 A. Kushima, X. Qian, P. Zhao, S. Zhang and J. Li, *Nano Lett.*, 2015, **15**(2), 1302–8.
- 23 T. H. Ly, J. Zhao, D. Keum, Q. Deng, Z. Yu and Y. H. Lee, *Nano Lett.*, 2016, **16**, 7807–7813.
- 24 R. V. Noorden, *Nature*, 2012, **483**, S32–S33.
- 25 H. Li, Q. Zhang, C. C. R. Yap, B. K. Tay, T. H. T. Edwin, A. Olivier and D. Baillargeat, *Adv. Funct. Mater.*, 2012, **22**, 1385–1390.
- 26 M. Samadi, N. Sarikhani, M. Zirak, H. Zhang, H.-L. Zhang and A. Z. Moshfegh, *Nanoscale Horizons*, 2018, **3**, 90–204.
- 27 G. Zhang, H. Liu, J. Qua and J. Li, *Energy Environ. Sci.*, 2016, **9**, 1190–1209.
- 28 X. Zhang, X.-F. Qiao, W. Shi, J.-B. Wu, D.-S. Jiang and P.-H. Tan, *Chem. Soc. Rev.*, 2015, **44**, 2757–2785.
- 29 X. Zhang, W. P. Han, J. B. Wu, S. Milana, Y. Lu, Q. Q. Li, A. C. Ferrari and P. H. Tan, *Phys. Rev. B*, 2013, **87**, 115413.
- 30 N. Dong, Y. Li, Y. Feng, S. Zhang, X. Zhang, C. Chang, J. Fan, L. Zhang and J. Wang, *Scientific Reports*, 2015, **5**, 14646.
- 31 J. Gruber, A. C. Lang, J. Griggs, M. L. Taheri, G. J. Tucker and M. W. Barsoum, *Scientific Reports*, 2016, **6**, 33451.
- 32 K. P. Dhakal, D. L. Duong, J. Lee, H. Nam, M. Kim, M. Kan, Y. H. Lee and J. Kim, *Nanoscale*, 2014, **6**, 13028–13035.
- 33 G. Eda, H. Yamaguchi, D. Voiry, T. Fujita, M. Chen and M. Chhowalla, *Nano Lett.*, 2011, **11**, 5111–5116.
- 34 T. Han, H. Liu, S. Wang, S. Chen, W. Li, X. Yang, M. Cai and K. Yang, *Nanomaterials*, 2019, **9**, 740.
- 35 K. F. Mak, K. He, C. Lee, G. H. Lee, J. Hone, T. F. Heinz and J. Shan, *Nature Mater*, 2013, **12**, 207–211.
- 36 M. M. Glazov, *J. Chem. Phys.*, 2020, **153**, 034703.
- 37 M. Palumbo, M. Bernardi and J. C. Grossman, *Nano Letters*, 2015, **15**, 2794–2800.
- 38 H.-L. Liu, T. Yang, J.-H. Chen, H.-W. Chen, H. Guo, R. Saito, M.-Y. Li and L.-J. Li, *Sci Rep*, 2020, **10**, 15282.
- 39 C. Zhang, H. Wang, W. Chan, C. Manolatou and F. Rana, *Phys. Rev. B*, 2014, **89**, 205436.
- 40 V. Le, T. Kim, H. Park, H. Nguyen, X. Nguyen and Y. Kim, *Current Applied Physics*, 2019, **19**, 182 – 187.
- 41 A. Arora, N. K. Wessling, T. Deilmann, T. Reichenauer, P. Steeger, P. Kossacki, M. Potemski, S. Michaelis de Vasconcellos, M. Rohlfing and R. Bratschitsch, *Phys. Rev. B*, 2020, **101**, 241413.
- 42 G. Berghäuser, P. Steinleitner, P. Merkl, R. Huber, A. Knorr and E. Malic, *Phys. Rev. B*, 2018, **98**, 020301(R).
- 43 L. V. Kotova, A. V. Platonov, V. N. Kats, V. P. Kochereshko, S. V. Sorokin, S. V. Ivanov and L. E. Golub, *Phys. Rev. B*, 2016, **94**, 165309.
- 44 L. V. Kotova, A. V. Platonov, V. P. Kochereshko, S. V. Sorokin, S. V. Ivanov and L. E. Golub, *Physics of the Solid State*, 2017, **59**, 2168–2173.
- 45 J. Wilson and A. Yoffe, *Advances in Physics*, 1969, **18**:73, 193–335.
- 46 R. F. Frindt and A. D. Yoffe, *Proceedings of the Royal Society of London. Series A, Mathematical and Physical Sciences*, 1963, **273**, 69–83.
- 47 J. V. Acrivos, W. Y. Liang, J. A. Wilson and A. D. Yoffe, *J. Phys. C: Solid State Phys*, 1971, **4**, L18.
- 48 R. Bailey, *Acta Cryst.*, 1950, **3**, 477.
- 49 Z. Hu, A. Singh, S. V. Goupalov, J. A. Hollingsworth and H. Htoon, *Nanoscale*, 2018, **10**, 22861–22870.
- 50 A. Laturia, M. L. V. de Put and W. G. Vandenberghe, *npj 2D Materials and Applications*, 2018, **2**, 6.
- 51 S. V. Gupalov, E. L. Ivchenko and A. V. Kavokin, *Journal of Experimental and Theoretical Physics*, 1998, **86**, 388–394.
- 52 M. M. Glazov, E. L. Ivchenko, O. Krebs, K. Kowalik and P. Voisin, *Phys. Rev. B*, 2007, **76**, 193313.
- 53 A. I. Prazdnichnykh, M. M. Glazov, L. Ren, C. Robert, B. Urbaszek and X. Marie, *arXiv:2010.01352*, 2020.
- 54 D. Kazanov, M. Rakhlin, A. Poshakinskiy and T. Shubina, *Nanomaterials*, 2020, **10**, 373.